Geophys. J. Int. (2007) **171,** 302–315 doi: 10.1111/j.1365-246X.2007.03510.x

Temperature distribution of the upper surface of the subducted Philippine Sea Plate along the Nankai Trough, southwest Japan, from a three-dimensional subduction model: relation to large interplate and low-frequency earthquakes

Shoichi Yoshioka[1] and Koji Murakami[2]

[1]*Department of Earth and Planetary Sciences, Faculty of Sciences, Kyushu University, Hakozaki* 6-10-1*, Higashi ward, Fukuoka* 812-8581*, Japan. E-mail: yoshioka@geo.kyushu-u.ac.jp*
[2]*Nippon Telegraph and Telephone West Corporation, Baba-cho* 3-15*, Chuo ward, Osaka* 540-8511*, Japan*

Accepted 2007 May 29. Received 2007 May 29; in original form 2006 April 3

SUMMARY

The Nankai subduction fault in southwest Japan is a plate boundary along which large megathrust earthquakes have repeatedly occurred. A previous 2-D thermal model suggested that the updip and downdip limits of the seismogenic zone are closely related to the temperature of the plate interface. We estimated a new temperature distribution for the plate interface based on a 3-D thermal convection model that incorporates revised governing equations, temporal changes in relative plate motion, the shape of the subducted slab, temperature variations related to basin evolution and more heat flow data and model regions than have been used in previous models. The margin-parallel spatial variation in the temperature of the plate interface was caused by spatio-temporal changes associated with the cooling of the Shikoku Basin. The updip limit of the thermally delineated seismogenic zone (thermal seismogenic zone) was approximately parallel to the trough axis due to a spreading rate that increased with distance from a fossil ridge, although the margin-parallel age dependency of the subducting plate was taken into account. The downdip limit of the thermal seismogenic zone was determined by temperature, except in eastern Kyushu, where it was determined by a boundary between the continental Moho depth and the upper surface of the subducting plate. The maximum coseismic slip associated with the 1944 Tonankai (M 7.9) and the 1946 Nankai (M 8.0) earthquakes, and a strongly coupled region estimated from GPS data inversion obtained by previous studies, were both located in the thermal seismogenic zone on the plate interface. Low-frequency earthquakes located at the downdip of the thermal seismogenic zone took place at temperatures of about 400–500 °C. This may be related to the phase transformation of hydrous minerals in oceanic crust from lawsonite + blueschist + jadeite to amphibole + eclogite and the associated decreases in water content of approximately 2.4 wt%. The thermal seismogenic zone is narrowest off the Kii Peninsula, where the hypocentres of the Tonankai and Nankai earthquakes were located. The narrow seismogenic zone may have determined the rupture initiation points for these earthquakes, as was previously demonstrated by numerical simulations of the earthquake cycle.

Key words: fossil ridge, large earthquake, low-frequency earthquakes, Nankai subduction fault, temperature distribution, thermal seismogenic zone.

GJI Seismology

1 INTRODUCTION

The Nankai Trough is a convergent plate boundary where the oceanic Philippine Sea (PHS) plate is subducting beneath the continental Amuria (AM) plate, which forms southwest Japan (Fig. 1). Megathrust earthquakes have occurred repeatedly on the Nankai subduction fault at intervals of approximately 90–150 yr (e.g. Ando 1975).

The seismogenic zones of plate boundaries are generally considered to be controlled by temperature; thus, temperature distributions on the upper surfaces of subducting oceanic plates in the circum-Pacific region have been the focus of much attention (e.g. Hyndman & Wang 1993; Hyndman *et al.* 1995; Oleskevich *et al.* 1999; Currie *et al.* 2002). According to Hyndman *et al.* (1995), the updip limit of such seismogenic zones coincides with a region where the temperature ranges from ∼100 to 150 °C, and where

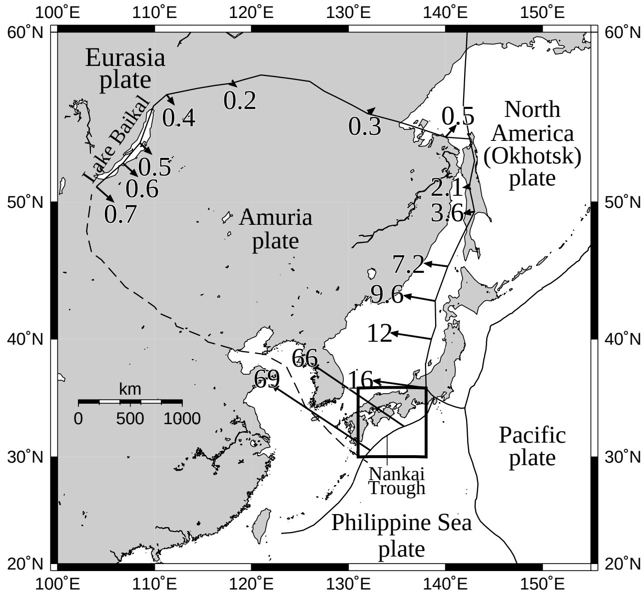

Figure 1. Tectonic map in and around the Japanese islands. Plate motion velocity vectors (mm yr^{-1}) of the AM plate relative to the adjacent plates are shown in numerals (Wei & Seno 1998). The dashed line is the plate boundary where the location is not clear. Heat flow data in the boxed region is shown in Fig. 2(a).

smectite, a clay mineral in the sedimentary layer, transforms into illite.

Hyndman *et al.* (1995) and Oleskevich *et al.* (1999) demonstrated that the temperature for the downdip limit of seismogenic zones ranges from 350 to 450 °C, based on a comparison of heat flow data at subduction zones and thermal models for oceanic plate subduction. Hyndman *et al.* (1997) proposed that the downdip limit of any seismogenic zone that does not reach such a temperature must correspond to a region where part of the mantle wedge is serpentinized. Shear strength in the serpentinized region would be very low, such that megathrust earthquakes could not occur. Low-frequency tremors and earthquakes with aseismic slow-slip events have occurred in the downdip extensions of the Nankai and Cascadia subduction zones (e.g. Dragert *et al.* 2001; Obara 2002; Katsumata & Kamaya 2003; Rogers & Dragert 2003; Obara & Hirose 2006), but temperature conditions related to their occurrence have not been determined, except for a 2-D case (Seno & Yamazaki 2003).

Hyndman *et al.* (1995) estimated the temperature distribution on the upper surface of the subducting PHS plate at the Nankai subduction zone. Since then, further information has become available. Seismic surveys and the amalgamation of hypocentre data from disparate research organizations have revealed the detailed shape of the subducting PHS plate (e.g. Nakamura *et al.* 1997; Kodaira *et al.* 2002). GPS data suggest that the continental plate involved is not the Eurasia (EU) plate, but the AM plate (e.g. Miyazaki & Heki 2001), indicating that boundary conditions for flow velocities and temperatures on the oceanic side should be modified. Hyndman *et al.* (1995) discussed the seismogenic zone of megathrust earthquakes off Shikoku and the Kii Peninsula based on the temperature of the upper surface of the subducting PHS plate and interseismic geodetic data. Because of a dramatic increase in heat flow data obtained from bottom-simulating reflectors (BSRs) off Shikoku and the Kii Peninsula (Ashi *et al.* 1999, 2002), it is now possible to carry out an analysis with much higher spatial resolution. To estimate the thermal distribution associated with the subduction of the PHS plate, Hyndman *et al.* (1995) solved the energy equation for a 2-D model. In contrast, we solve equations for conservation of mass, momentum, and energy as a coupled problem, using a 3-D model and taking induced flow in the mantle wedge into account. Although such a calculation was carried out by Furukawa (1999) for the Nankai subduction zone, his model was 2-D and focused only on a profile through the Kii Peninsula. Another factor to be considered is the margin-parallel age dependency of the Shikoku Basin floor, which can be identified from the spatial distribution of heat flow data. We present a new 3-D temperature distribution for the upper boundary of the subducted PHS plate in southwest Japan and clarify its relation to large interplate and low-frequency earthquakes.

2 HEAT FLOW DATA IN AND AROUND SOUTHWEST JAPAN

We compiled heat flow data from borehole and heat-probe measurements (Tanaka *et al.* 2004) and BSR-based estimates (Ashi *et al.* 1999, 2002) for 355 and 1542 data points, respectively (Fig. 2). Profiles roughly parallel to the trough axis indicate that heat flow values are high near a fossil spreading ridge and decrease gradually and symmetrically with increasing distance (Fig. 2b). A similar tendency occurs along a more landward profile roughly

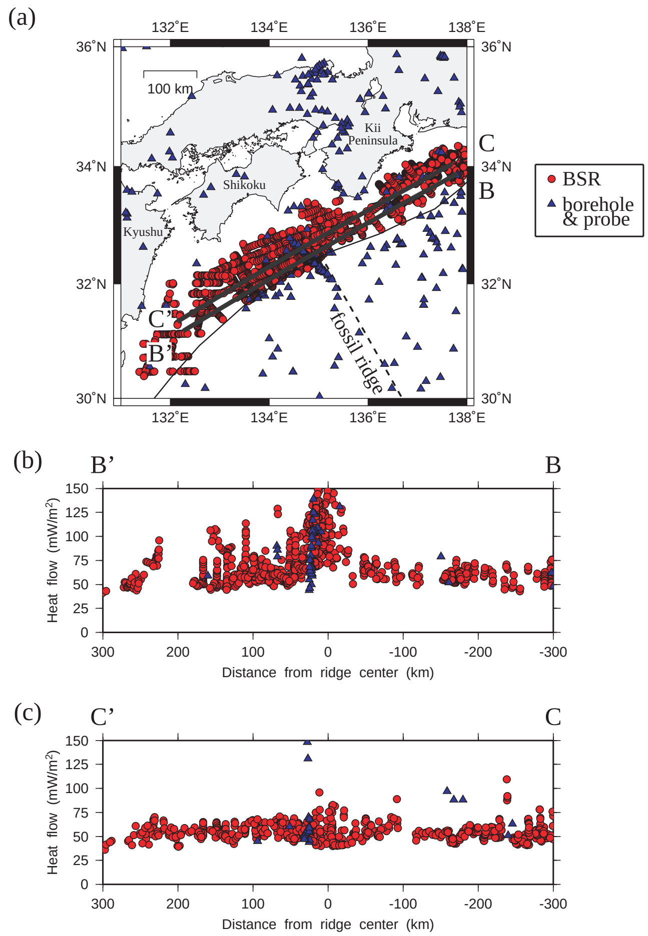

Figure 2. (a) Spatial distribution of heat flow data in and around southwest Japan. Red circles and blue triangles denote BSR (Ashi *et al.* 1999, 2002), and borehole data on land and marine heat probe data (Tanaka *et al.* 2004), respectively. (b) Heat flow data along the profile B–B′ in (a). All the data within 30 km on both sides of the profile are plotted. (c) Heat flow data along the profile C–C′ in (a).

parallel to the trough axis (Fig. 2c). We assume that this decrease in heat flow with increasing distance from the fossil ridge is attributed to the age dependency of the subducting PHS plate. Heat flow data along the profile B–B′, which is located close to the trough axis, are scattered, probably because of the effect of hydrothermal fluid circulation. Data along the profile C–C′ are more consistent. We attempted to fit the heat flow values that we obtained by numerical modelling to heat flow data along the margin-parallel profile C–C′ as well as margin-normal profiles.

3 SUBDUCTION HISTORY OF THE PHS PLATE

The PHS plate is subducting along the Nankai Trough beneath the AM plate, which includes the continental part of southwest Japan. The relative plate motion of the AM-PHS convergence zone has been determined using GPS data (Sella *et al.* 2002).

Following Wang *et al.* (1995), we assumed that the subduction of the PHS plate along the Nankai Trough initiated at 15 Ma. According to Seno & Maruyama (1984), the PHS plate changed its direction of motion relative to the continental plate from NNW to NW during the interval from 10 to 5 Ma. Based on the geological structure of the Baikal rift, located on the northwestern boundary of the AM plate (Fig. 1), Mats (1993) concluded that the Baikalian arch developed after 3.5 Ma by the deepening and spreading of depressions. Based on the age of the Kurotaki unconformity near the Boso Peninsula, central Japan, Takahashi (2004) suggested that the location of the Euler pole of the PHS plate changed at 3 Ma from east of the triple junction connecting the Japan trench, the Izu-Bonin trench, and the Sagami trough, to northeast of Hokkaido, north Japan. We considered that the change was partly caused by the separation of the AM plate from the Eurasia (EU) plate at 5 Ma and assumed that the PHS plate was not subducting beneath the current AM plate from 15 to 5 Ma, but beneath the EU plate. The relative plate motion for this interval is not known, so velocity vectors were assumed to be parallel to the fossil ridge and constant (4.0 cm yr^{-1}) along the Nankai Trough (Fig. 3c). Bathymetric data indicate that the fossil ridge trended $\sim 330^{\circ}$ (Sandwell & Smith 2000).

The age of the subducting PHS plate is one of the factors controlling the temperature distribution in the subduction zone. The PHS plate underlies the Shikoku Basin at its northern end, which formerly spread in an ENE–WSW direction, away from the fossil spreading ridge (e.g. Okino *et al.* 1994) (Fig. 3a). Subduction of the fossil ridge in the PHS plate along the Nankai Trough is roughly parallel to the ridge's trend, so the age of the PHS plate at the Nankai Trough increases with both elapsed time (e.g. Wang *et al.* 1995) and margin-parallel distance from the fossil ridge. To calculate temperatures on the plate interface, it is necessary to know the spreading rate of the Shikoku Basin prior to 15 Ma. An optimal local spreading rate that best fit the heat flow data for the margin-parallel profile investigated was determined by trial-and-error.

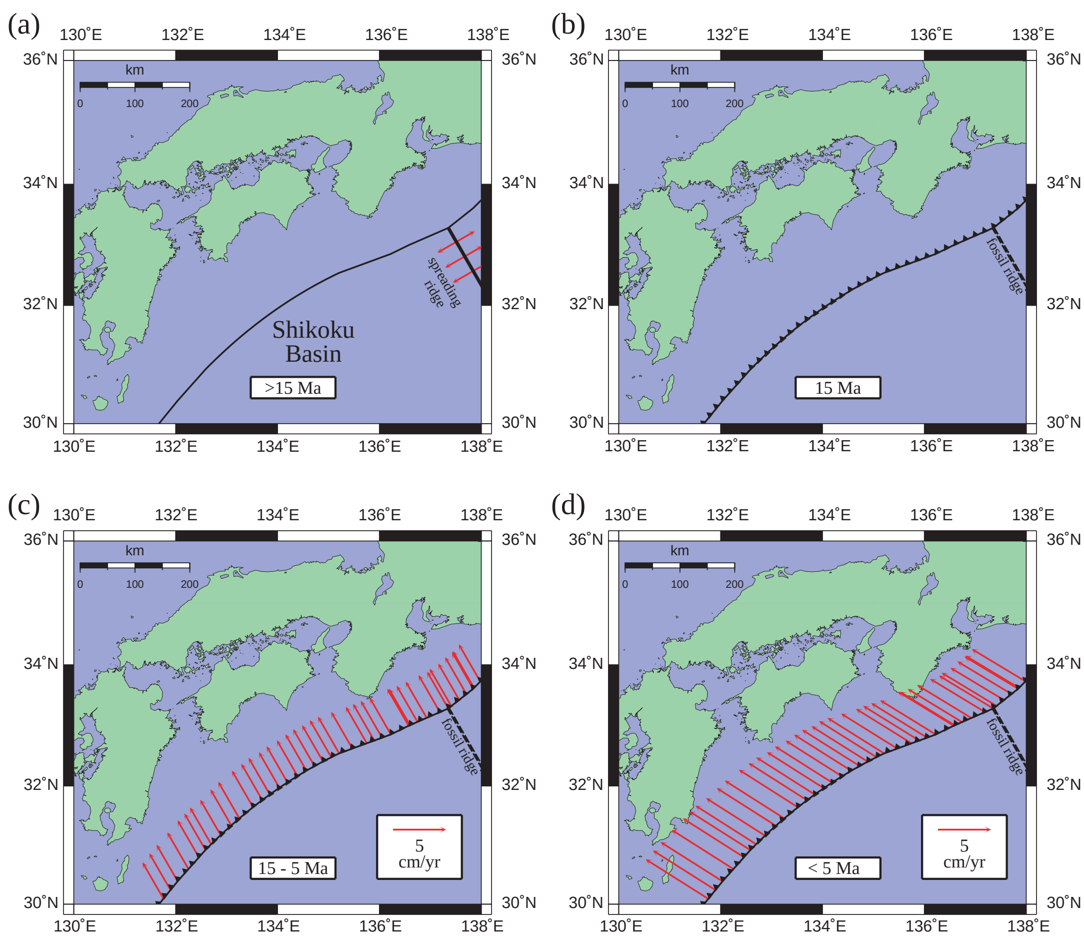

Figure 3. Assumed subduction history in southwest Japan. (a) Time stage before 15 Ma. (b) Time stage at 15 Ma. (c) Time stage from 15 to 5 Ma. The red arrows indicate plate motion velocity vectors of the PHS plate relative to the continental plate along the Nankai Trough. (d) Time stage from 5 Ma to the present. For details, see the text.

The following subduction history is indicated.

(1) The Shikoku Basin formed by ENE–WSW spreading away from the now defunct ridge until 15 Ma (Fig. 3a).

(2) Shikoku Basin spreading ceased at 15 Ma, leaving the fossil ridge in its centre (Fig. 3b).

(3) The PHS plate began to subduct along the Nankai Trough beneath the EU plate in a direction parallel to the trend of the fossil ridge with a constant velocity of 4.0 cm yr^{-1} (Fig. 3c).

(4) The PHS plate changed the direction of relative plate motion northwestward at 5 Ma, which was partly caused by eastward motion of the AM plate resulting from its separation from the EU plate at 5 Ma. As a result, the PHS plate began to subduct obliquely beneath the AM plate along the Nankai Trough (Fig. 3d).

(5) The subduction velocity increased from 4.0 cm yr^{-1} to the present rate over the last 5 Myr. The location of the fossil ridge moved westward due to oblique subduction until reaching its current position.

4 A 3-D THERMAL CONVECTION MODEL

4.1 Model configurations and governing equations

The spatio-temporal distribution of temperature and flow velocity associated with the subduction of the PHS plate along the Nankai Trough were calculated using a 3-D Cartesian box model with finite-difference and control volume methods (Fig. 4). The 3-D convection code 'Stag3d' of Tackley (1996) was modified so that it could be used for subduction zones. The *y*-axis was aligned with the trend of the local trough axis, and the *x*- and *z*-axes were horizontal and vertical, respectively. The continental plate consisted of an accretionary prism, upper and lower crust and underlying upper mantle, whereas the oceanic plate consisted of the subducting slab, including the fossil ridge and the upper mantle beneath. The accretionary prism was taken to a horizontal distance of 90 km landward from the trough axis (Hyndman *et al.* 1995). The thicknesses of the upper and lower crusts of the continental plate were both assumed to be 16 km, and composed of rigid, conductive layers assigned a zero-velocity condition, which restricts them from participating in the viscous flow region. The length of the subducted slab increased with time since the initiation of subduction, and induced flow took place in the mantle wedge. To reduce the effect of the model's lower boundary, its position was set at a depth of 400 km. The horizontal length of the model parallel to the local trough axis (*y*-axis) was 400 km, and the horizontal length perpendicular to the local trough axis (*x*-axis) was variable, depending on the dip angle. The model was descretized into 96 × 96 × 96 elements. The plate interface was a flat plane for which the local dip angle coincided with that at a central cross-section bisecting the 3-D model space in the *y*-direction.

An anelastic approximation was used, and the theoretical formulation follows the notation of Honda (1997). In the following, the suffixes 0 and z refer to the model surface and a depth of z, respectively, and s indicates adiabatic conditions. 3-D Cartesian coordinates (x, y, z) are represented by (x_1, x_2, x_3). The equation of mass conservation is given by

$$\nabla \cdot [\rho_s(z)\mathbf{v}] = 0, \tag{1}$$

where $\rho_s(z)$ and $\mathbf{v} = (v_1, v_2, v_3)$ are density and flow velocity vectors, respectively. The ρ_s is given by

$$\frac{1}{\rho_s}\frac{d\rho_s}{dx_3} = -\frac{Di_z}{\Gamma_z}. \tag{2}$$

Here, Di_z and Γ_z are the dissipation number and the Grüneisen number, respectively, defined as

$$Di_z = \frac{g\alpha D}{C_{p0}} \tag{3}$$

and

$$\Gamma_z = \frac{\alpha K_{T0}}{\rho_s C_{v0}}, \tag{4}$$

where g is gravity acceleration, α is thermal expansivity, D is the model thickness, C_{p0} is specific heat at constant pressure, K_{T0} is

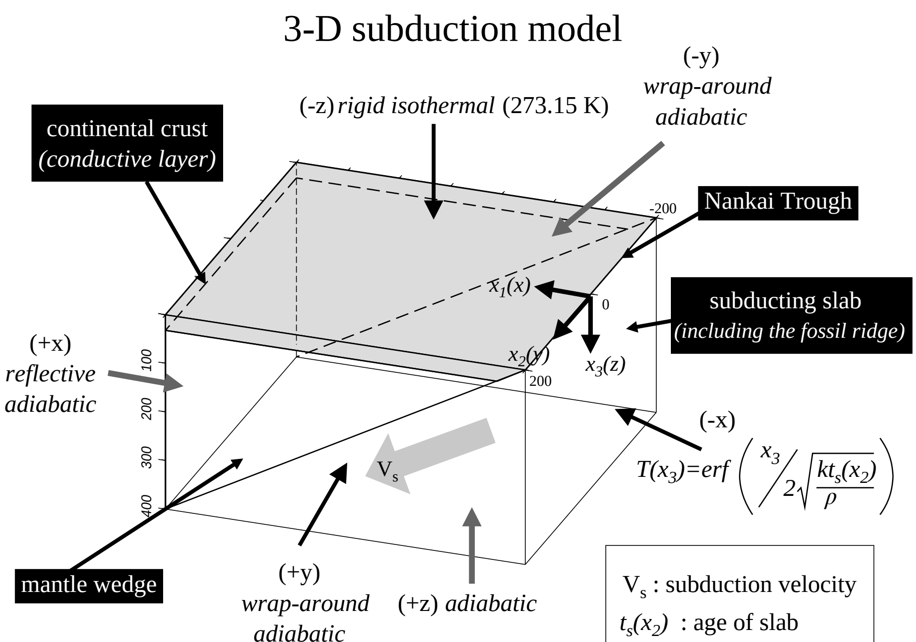

Figure 4. Schematic figure showing the 3-D parallelepiped model used in this study. For details, see the text.

the isothermal bulk modulus, and C_{v0} is specific heat at constant volume. The momentum equation is given by

$$-\frac{\partial P}{\partial x_i} + \frac{\partial \tau_{ij}}{\partial x_j} + Ra_0 \alpha (T - T_s)\delta_{i3} = 0, \quad (5)$$

where P is a pressure deviation from hydrostatic pressure, τ_{ij} is a stress tensor, T is temperature and δ_{ij} is the Kronecher's Delta. T_s can be represented by

$$\frac{dT_s}{dx_3} = Di_z T_s. \quad (6)$$

Ra_0 is the Rayleigh number, which is given by

$$Ra_0 = \frac{g\alpha_0 D^3 \Delta T}{\upsilon_0 \kappa_0}, \quad (7)$$

where ΔT is the temperature difference between the top and bottom model boundaries, and υ_0 and κ_0 are dynamic viscosity and thermal diffusivity, respectively. Thermal expansivity α can be expressed by the density-dependent equation of Chopelas & Boehler (1992)

$$\alpha = \alpha_0 \exp\left\{-4.3\left[1 - \left(\frac{\rho_0}{\rho}\right)^{1.4}\right]\right\}. \quad (8)$$

The density ρ depends on temperature, such that

$$\rho = \rho_s[1 - \xi\alpha(T - T_s)], \quad (9)$$

where ξ is the product of α_0 and ΔT. For viscosity μ, the following temperature- and depth-dependent form of Christensen (1996) was used:

$$\mu = \mu_0 \exp\left[\frac{1-T}{0.097} + \frac{x_3}{0.59} - \left(\frac{x_3}{2.72}\right)^2\right]. \quad (10)$$

The energy equation can be expressed by

$$\rho C_{p0}\left(\frac{\partial T}{\partial t} + \mathbf{v}\cdot\nabla T\right) + Di_0 \rho_s \alpha v_3 T$$
$$= \nabla\cdot(k\nabla T) + \frac{Di_0}{Ra_0}\tau_{ij}\varepsilon_{ij} + Rh_0 \rho Rh, \quad (11)$$

where Rh is internal heating per unit mass, Di_0 is the dissipation number, and Rh_0 is a non-dimensionalized parameter representing internal heating; they are given by

$$Di_0 = \frac{g\alpha_0 D}{C_{p0}} \quad (12)$$

and

$$Rh_0 = \frac{\rho_0 Rh_{\mathrm{mantle}} D^2}{k_0 \Delta T}. \quad (13)$$

In eq. (11), the density ρ of the crust has a constant value without following eq. (9), and k and Rh take different constant values, depending on domains in the model (Table 1). Using MPDATA (Smolarkiewicz 1984), the advection term in eq. (11) is solved. Values for model parameters are provided in Table 2.

Based on the difference in directions between geodetically obtained margin-normal contraction and seismically obtained margin-parallel compressive stress, and the 2-D finite-element modelling of stress fields, Wang (2000) suggested that the subduction fault in southwest Japan is very weak. This is consistent with geothermal data that require very low frictional heating along the subduction fault. For this reason, possible frictional heating at the plate interface was not included in the model.

Table 1. Thermal properties used for the temperature calculations.

Geological unit	Thermal conductivity $\mathrm{Wm^{-1}\,k^{-1}}$	Heat production ($\mathrm{W\,k^{-1}}$)	Density ($\mathrm{kg\,m^{-3}}$)
Upper crust (0–16 km)	2.5[a]	7.3×10^{-10a}	2600[a]
Lower crust (16–32 km)	2.5[a]	1.4×10^{-10a}	2900[a]
Mantle and oceanic plate	2.5	2.245×10^{-13a}	3300[a]
Accretionary prism	1.4[b]	7.3×10^{-10a}	2600[a]

[a]Wang *et al.* (1995).
[b]Ashi *et al.* (2002).

4.2 Initial and boundary conditions and 3-D models

Boundary conditions for flow velocity are rigid at the interface between the lower crust and the mantle, reflective at the $+x$ plane, and wrap around at the $-y$ and $+y$ planes (Fig. 4). Subducting velocity vectors $\mathbf{v}_s$ at the $-x$ and $+z$ planes can be expressed by

Table 2. Thermodynamic parameters and values used in this study.

Parameters	Symbol	Value	Units	Non-D value
Non-dimensional parameters				
Surface Rayleigh number	Ra_0			1.4×10^6
Surface dissipation number	Di_0			0.05
Surface Grüneisen number	Γ_0			1.0
Product of thermal expansivity and temperature difference ΔT	ξ			0.0405
Non-dimensional number expressing radioactive heating	Rh_0			0.007
Nominal dimensional parameters				
Temperature difference between the top and bottom model boundaries	ΔT	1300	°C	1.0
Standard density	ρ_0	3300[a]	$\mathrm{kg \cdot m^{-3}}$	1.0
Standard thermal expansivity	α_0	3.0×10^{-5b}	$\mathrm{K^{-1}}$	1.0
Standard thermal conductivity	k_0	2.9[c]	$\mathrm{Wm^{-1}\,k^{-1}}$	1.0
Standard viscosity	η_0	1.0×10^{20c}	Pa s	1.0
Standard specific heat at constant pressure	C_p	1200[a]	$\mathrm{J\,kg^{-1}\,K^{-1}}$	1.0
Depth of the model	D	400	km	1.0
Radioactive heat production in the mantle	Rh_{mantle}	2.245×10^{-13a}	$\mathrm{W\,kg^{-1}}$	1.0

[a]Wang *et al.* (1995).
[b]Iwamori (1997).
[c]Christensen (1996).

$$\mathbf{v}_s = (v_{s1}, v_{s2}, v_{s3}) = v_{\mathrm{OBS}}[\cos(\varphi - \lambda)\cos\theta, \sin(\varphi - \lambda)\cos\theta, \times \cos(\varphi - \lambda)\sin\theta] \times {}^{\kappa_0}\!/_{D}, \quad (14)$$

where v_{OBS} represents the velocity of the PHS plate relative to the AM plate, φ represents the direction of relative plate motion, λ represents the x-axis orientation in the model, and φ represents the dip angle. The values of φ and λ are measured anticlockwise from the north. For simplicity, subducting velocities apply to the whole region of the lower trigonal pyramid, for which the upper part can be regarded as the subducting slab.

Initial thermal conditions are based on a layered, 1-D temperature field for the entire model domain. We used the following equation (Yoshioka & Sanshadokoro 2002):

$$T = \mathrm{erf}\left(\frac{x_3}{2\sqrt{\frac{kt_{\mathrm{cont}}}{\rho}}}\right) \quad (15)$$

where

$$t_{\mathrm{cont}} = \left(\frac{z_{\mathrm{cont}}}{7.5}\right)^2 \times {}^{\kappa_0}\!/_{D^2}, \quad (16)$$

and z_{cont} corresponds to the thickness of the continental lithosphere. This equation was originally used for the cooling of an oceanic plate (Yoshii 1975). Although heat flow data on land are affected by the initial temperature distribution, they are scattered for different margin-normal profiles. An initial temperature distribution was determined so that the calculated heat flow fitted the average of the observed heat flow data along the margin-normal profile passing through the central Kii Peninsula, which, of the investigated margin-normal profiles on land, has the greatest number of heat flow data points. The best-fitting heat flow value was obtained when z_{cont} was set at 48 km.

Temperature boundary conditions are isothermal (273.15 K) at $-z$ and adiabatic at the $+x$, $-y$, $+y$, and $+z$ planes (Fig. 4). The temperature boundary condition of the subducting PHS plate at the $-x$ plane can be given by the cooling of the oceanic plate,

$$T = \mathrm{erf}\left(\frac{x_3}{2\sqrt{\frac{kt_s(x_2)}{\rho}}}\right), \quad (17)$$

where $t_s(x_2)$ is the age of the subducting PHS plate at an arbitrary position along the Nankai Trough.

Given that ridge subduction takes place along the Nankai Trough, the age of the subducting slab is specified by the sum of the elapsed time since the initiation of subduction and the age of the oceanic slab, which depends on the margin-parallel distance from the fossil ridge, that is, the shorter the distance from the fossil ridge, the younger the age of the subducting plate. The oceanic plate was assumed to be subducting beneath the continental EU plate from 15 to 5 Ma (0–10 Myr in the model) in a direction parallel to the strike of the fossil ridge, so the margin-parallel distance from the fossil ridge to an arbitrary position on the y-axis was constant during that time, and the age of the slab at the trough axis increased at the same rate as the elapsed time since the initiation of subduction. The age of the slab at the trough axis can be represented by

$$t_s(x_2) = \left[t_{\mathrm{calc}} + \frac{|y_{\mathrm{ridge}}(t_{\mathrm{calc}}) - x_2|}{v_{\mathrm{ridge}}}\right] \times \kappa_0/D^2 \quad (t_{\mathrm{calc}} < 10\ \mathrm{Myr}), \quad (18)$$

where t_{calc} is the elapsed time, $|y_{\mathrm{ridge}}(t_{\mathrm{calc}}) - x_2|$ is the margin-parallel distance at an arbitrary position x_2 from the fossil ridge, which is constant during the period from 15 to 5 Ma, and v_{ridge} is the local spreading rate of the Shikoku Basin before 15 Ma. Given that the subduction direction was assumed to have coincided with the relative plate motion of the PHS and AM plates from 5 Ma to the present (10–15 Myr), the distance $|y_{\mathrm{ridge}}(t_{\mathrm{calc}}) - x_2|$ changes as a function of oblique subduction during that time, and the age of the slab can be represented by

$$t_s(x_2) = \left[t_{\mathrm{calc}} + \frac{|y_{\mathrm{ridge}}(t_{\mathrm{calc}}) - \int_{10}^{t_{\mathrm{calc}}} v_{s2}\,\mathrm{d}t - x_2|}{v_{\mathrm{ridge}}}\right] \times \kappa_0/D^2 \quad (t_{\mathrm{calc}} \geq 10\ \mathrm{Myr}). \quad (19)$$

We assumed that the plate velocity increased gradually from 4.0 cm yr^{-1} at 5 Ma to v_{OBS} at present.

In an example of the age of the subducting plate along the trough axis for a model region that includes the eastern part of Shikoku (Fig. 5), a half-spreading rate of 2.0 cm yr^{-1} was used so that the calculated heat flow fitted the gradient and amplitude of the observed heat flow away from the centre of the fossil ridge along the margin-parallel profile C–C′ (Fig. 2c). The trough of each V-shaped line (Fig. 5) represents the location of the fossil ridge at each time. The ridge's location did not move with respect to the Nankai Trough until 10 Myr, after which it moved westward from 10 to 15 Myr due to the effect of oblique subduction (eqs 18 and 19). It reached its present position (distance = 0 km) at 15 Myr. In estimating the age of the Shikoku Basin, however, the spreading rate is valid only within about 70 km of its centre because adjacent model regions, including

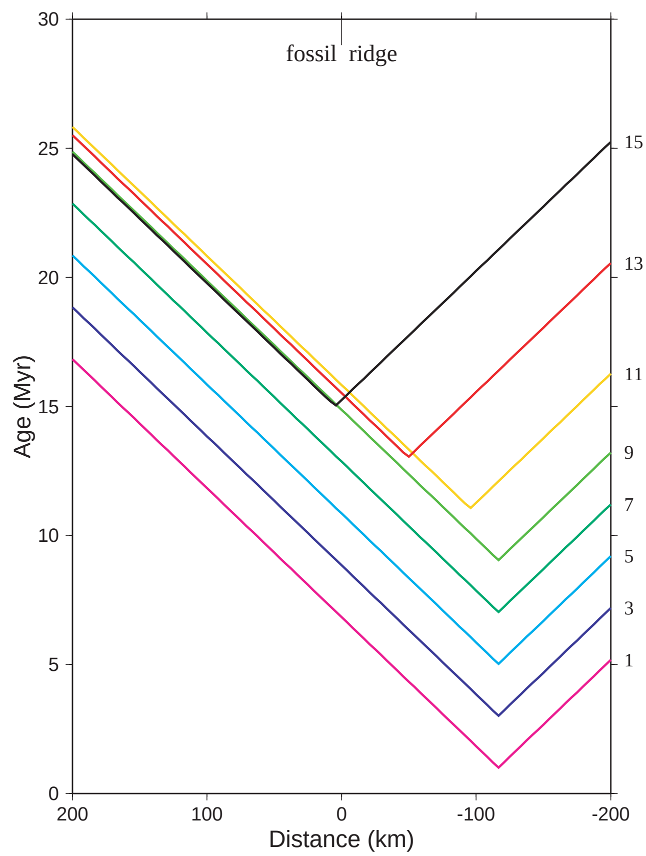

Figure 5. Age history of the subducting PHS plate for model region 4 in Fig. 6. Half-spreading rate before 15 Ma is 2.0 cm yr^{-1}. Horizontal and vertical axes represent y coordinate in Fig. 7 and age of the subducting plate at the $-x$ boundary, respectively. Each V-shaped line represents the age of the subducting plate at the same elapsed time labelled on the right.

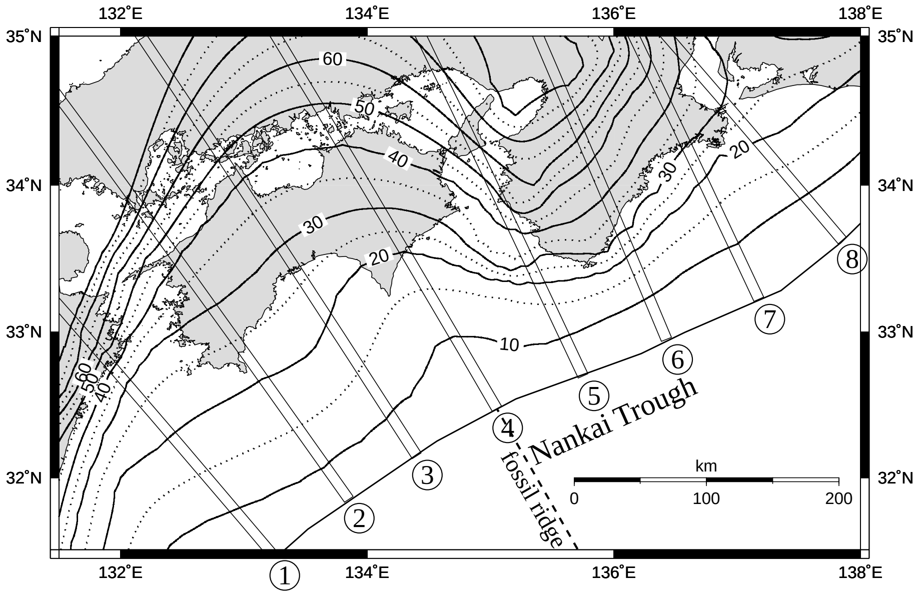

Figure 6. Isodepth contours of the upper surface of the subducting PHS plate along the Nankai Trough estimated from the results by Nakamura *et al.* (1997), Baba *et al.* (2000), Shimizu *et al.* (2000) and Kodaira *et al.* (2002). Contour interval is 5 km. The numbered eight paired regions bounded by thin solid lines almost perpendicular to the trough axis are used to obtain temperature distribution on the plate interface (Fig. 10). These are located central part of each 3-D parallelepiped model, bisecting the model region in the *y* direction (Fig. 4).

adjacent cross-sections spaced at about 70 km, have half-spreading rates that are not 2.0 cm yr^{-1}.

On the basis of hypocentre distributions (Nakamura *et al.* 1997; Shimizu *et al.* 2000) and seismic surveys (Baba *et al.* 2000; Kodaira *et al.* 2002), the 3-D shape of the upper surface of the subducting PHS plate was established for the purposes of modelling (Fig. 6). Ideally, a single 3-D model that incorporates the complicated 3-D slab shape could be applied to all of southwest Japan, but because the fluid flow associated with the subducting slab is given kinematically, it is almost impossible to satisfy conditions for 3-D flow and mass conservation with a slab that has a complex 3-D shape. In other words, because the flow velocities must be cited with three different components for each gridpoint, it is a formidable task to satisfy the mass conservation equation for all of the control volumes, even if an anelastic approximation is used. As a result, it is impossible to obtain a stable solution for such a problem.

Instead, southwest Japan was divided into eight smaller regions with different local dip angles, assuming a flat plane for each local plate interface. The plane shapes and dispositions fit the previously determined 3-D slab configuration well to a depth of about 60–70 km along the margin-normal profiles passing through eastern Shikoku and the Kii Peninsula. In this approach, fluid flows at slab gridpoints are parallel to each other, so the mass conservation equation can be readily satisfied. The temperature distribution on the plate interface was determined by interpolating the calculated results for the eight model regions (Fig. 6). The PHS plate is subducting beneath Shikoku at an angle of less than 10°. The dip of the PHS plate beneath the Kii Peninsula is slightly higher than that beneath Shikoku.

5 RESULTS

5.1 Comparison of observed and calculated heat flow

We calculated the spatial distributions of temperature and flow velocities associated with the subduction of the PHS plate in the *x–z* plane at 0 Ma (15 Myr) along the profile A–A′ passing through eastern Shikoku (Fig. 7). The results were obtained for model region 4 (Fig. 6). Because of the low dip angle and short time since the initiation of subduction, seaward flow in the mantle wedge is not remarkable. The calculated heat flow along the profile decreases slightly landward to about 55 mW m^{-2} (Fig. 7c), then increases gradually, reaching a constant of about 80 mW m^{-2} at a horizontal distance of about 300 km from the trough axis. The calculated heat flow agreed well with the observed heat flow data both in amplitude and spatial pattern.

Fig. 8(b) shows temperature and flow velocity fields in the *y–z* plane at 0 Ma (15 Myr) along the profile C–C′, which is almost parallel to the local trough axis. Given the assumption of axisymmetrical plate cooling perpendicular to the trend of the fossil ridge, the hottest region would be located just below the fossil ridge. In view of the oblique subduction, flow velocity vectors were oriented westward with a downward component in the *y–z* plane. The calculated heat flow along the profile has a maximum of about 65 mW m^{-2} near the fossil ridge, and decreases gradually with increasing margin-parallel distance from the fossil ridge (Fig. 8c), corresponding to the temperature field in Fig. 8(b). The half-spreading rate of 2.0 cm yr^{-1} was used so that the calculated heat flow fitted the gradient and amplitude of the data away from the centre of the fossil ridge. By constructing an elastic flexure model to accommodate margin-normal bathymetry data corrected for thick sediment effects, Yoshioka & Ito (2001) demonstrated that the effective elastic plate thickness is thin near the fossil ridge and increases gradually with increasing margin-parallel distance from the fossil ridge. The calculated thermal state (Fig. 8b) is consistent with their results.

Fig. 9 shows temperature and flow velocity fields for a vertical cross-section along the profile A–A′, which passes through the Kii Peninsula. The results were obtained for model region 6 (Fig. 6). The dip angles of the subducting PHS plate below the Kii Peninsula are slightly higher than those below Shikoku (Fig. 6). As a result, seaward high-temperature flow from the backarc region tends to take place more easily in the mantle wedge (outside the

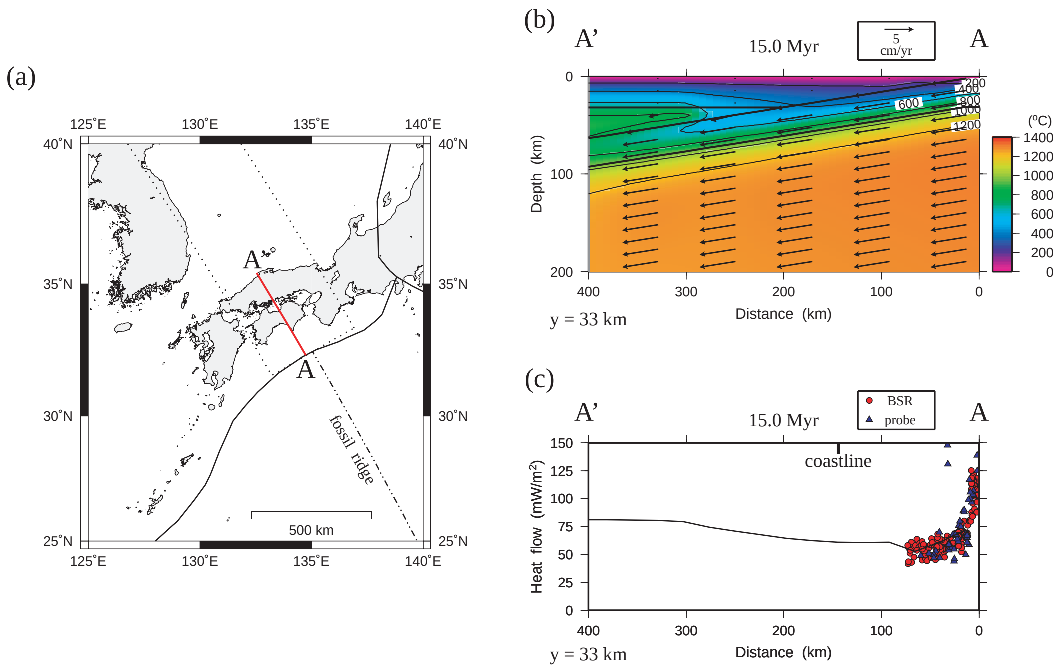

Figure 7. (a) Map view showing the location of a 3-D model (dotted lines) (model region 4 in Fig. 6). The profile A–A′ is located slightly west of the NNW extension of the strike of the current fossil ridge, as well as almost bisects the model space in the *y*-direction (400 km) along the trough axis. (b) Temperature (colour) and flow velocity (arrows) fields in the vertical cross-section passing through the profile A–A′ in (a) at 15 Myr (0 Ma). (c) Comparison between observed and calculated (solid line) heat flow along the profile A–A′ in (a) at 15 Myr (0 Ma). Red circles and blue triangles denote BSR and marine heat probe data, respectively. All the data within 30 km on both sides of the profile are plotted.

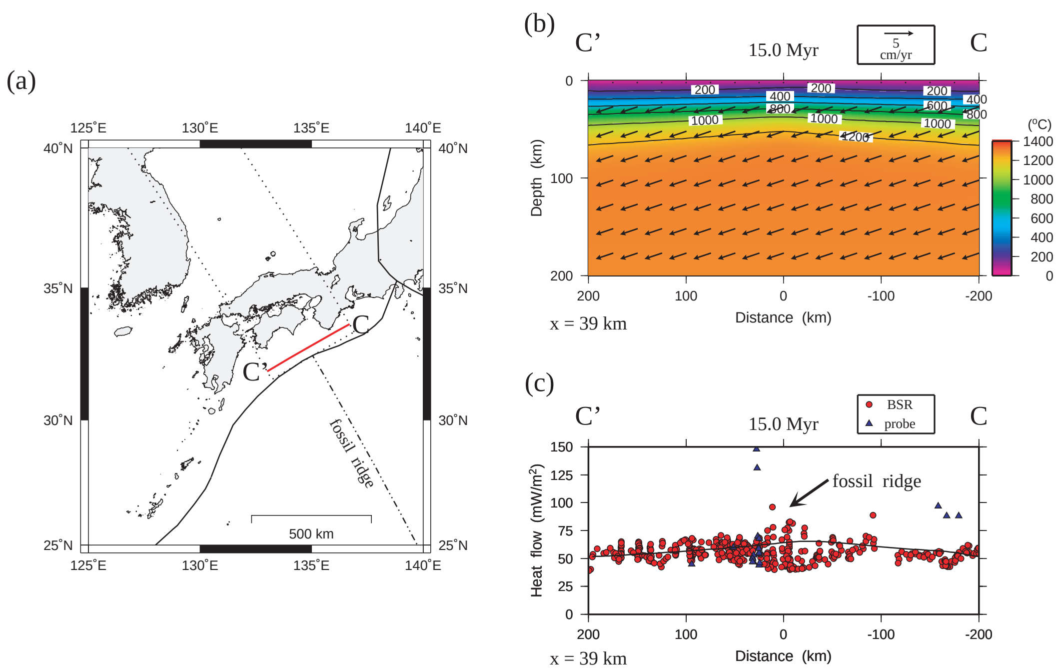

Figure 8. (a) Map view showing the location of the same 3-D model as Fig. 7 (dotted lines). The profile C–C′ is 39 km away from the $-x$ plane in the $+x$ direction in Fig. 4. (b) Temperature (colour) and flow velocity (arrows) fields in the vertical cross-section passing through the profile C–C′ in (a) at 15 Myr (0 Ma). (c) Comparison between observed and calculated (solid line) heat flow along the profile C–C′ in (a) at 15 Myr (0 Ma). Red circles and blue triangles denote BSR and marine heat probe data, respectively. All the data within 30 km on both sides of the profile are plotted.

plotted range), and hot material reaches as far as its seaward corner. The dramatic change in the calculated heat flow along the profile at a horizontal distance of about 90 km is caused by the different values assumed for the thermal conductivity of the accretionary prism and the upper crust (Fig. 9c; Table 1). The calculated results fit the observations well, except for some low heat flow data at a horizontal distance of approximately 200 km. These data are located on the Osaka Plain, which is covered by several

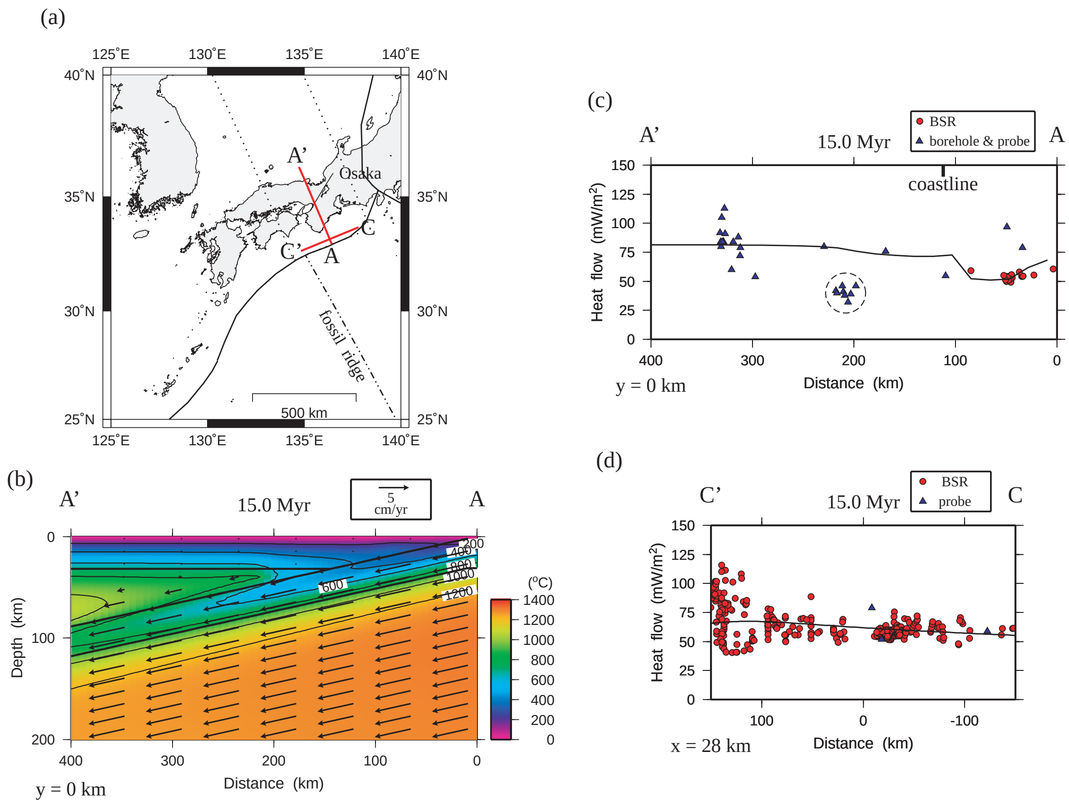

Figure 9. The same as Figs 7 and 8 except for location of the 3-D model, the dip angle, temperature boundary condition on the $-x$ plane (model region 6 in Fig. 6). The heat flow data encircled by the dashed line in (c) are located in Osaka Plain. Blue triangles denote borehole data on land in addition to marine heat probe data in (c).

hundred meters of post-Pleistocene sediments that cause the local low heat flow values (Hyndman *et al.* 1995). The calculated heat flow also fitted the observations well along the profile C–C′ (Fig. 9a and d). Based on the gradient and amplitude away from the centre of the fossil ridge, the half-spreading rate of the Shikoku Basin off the Kii Peninsula before 15 Ma was determined to have been 3.0 cm yr^{-1}.

In Figs 7 and 9, the 3-D parallelepiped box model was oriented so that its centre passed through eastern Shikoku and the Kii Peninsula, and 3-D temperatures, flow velocities, and heat flow were then calculated for the respective model regions. The dip angles of the subducting plate were taken from the values along the central parts of the respective models, bisecting each model region in the *y* direction.

Temperatures, flow velocities, and heat flow along the margin-normal and margin-parallel profiles were calculated for the six other model regions (Fig. 6), yielding subduction parameters such as v_{OBS}, θ, φ and λ, as well as different temperature boundary conditions at the $-x$ plane, which arise from differences in the relative location of the fossil ridge in the respective models. The observed heat flows for the six regions can be generally explained by calculations along both profiles A–A′ and C–C′. Based on the local half-spreading rates for the eight profiles along C–C′, the age of the Shikoku Basin floor can be estimated along the length of the Nankai Trough. The age of the oceanic plate at the east flank of the Kyushu-Palau Ridge, located approximately 290 km WSW of the fossil ridge, was estimated at approximately 25.6 Ma, which coincides well with that estimated from magnetic anomalies (26 Ma; Kobayashi & Nakada 1978; Okino *et al.* 1994). The model is, therefore, consistent with both the present margin-parallel heat flow data and the age of the Shikoku Basin estimated from fossil magnetic anomalies. Another interesting feature is that the spreading rate that we estimated tends to increase gradually with increasing margin-parallel distance from the fossil ridge, ranging from 2.0 to 4.0 cm yr^{-1}. This indicates that the spreading rate of the Shikoku Basin was faster at earlier than at later stages, which is also consistent with magnetic anomaly evidence (Okino *et al.* 1994).

5.2 Calculated temperature distribution on the upper surface of the subducting PHS plate

Temperatures at the upper surface of the PHS plate were calculated by interpolating the margin-normal temperature distributions at the plate interface in the central part of each of the eight model regions (Fig. 10). On the basis of this thermal model, we discuss the distribution of seismogenic zones. Plate interfaces in the temperature range of 150–350 °C are referred to as the 'thermal seismogenic zone,' and those from 350 to 450 °C belong to the 'transition zone.'

The calculated results show that isothermal contours have margin-parallel lateral variations, whereas the updip temperature limit of the thermal seismogenic zone is roughly parallel to the trough axis. The temperature of the deeper part of the plate interface is not symmetrical away from the fossil ridge. The thermal seismogenic zone is narrowest off the Kii Peninsula and widens both eastward and westward because of spatial differences in the dip angle and the former location of the fossil ridge.

The uncertainty of the temperature distribution on the plate interface was investigated, taking into account observation errors in heat

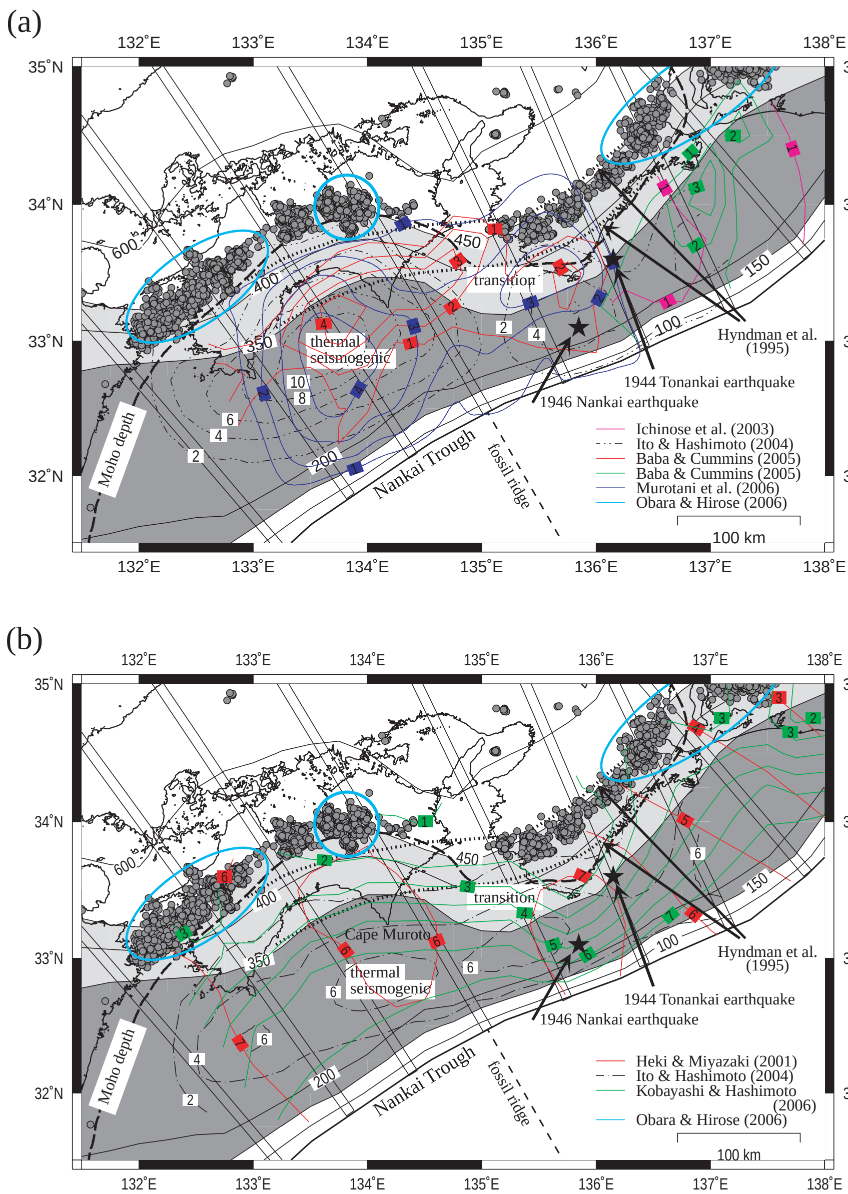

Figure 10. Estimated temperature distribution on the upper surface of the subducting PHS plate. Temperature ranges of 150–350 °C and 350–450 °C correspond to the thermal seismogenic (dark grey) and transition (light grey) zones, respectively. The two dotted lines are isotherms of 350 and 450 °C, respectively, on the plate interface estimated by Hyndman *et al.* (1995). The thick dashed line represents the boundary line between the continental Moho depth (32 km) and the upper surface of the subducting PHS plate. The hypocentres of the 1944 Tonankai and the 1946 Nankai earthquakes are shown with solid stars. Small solid circles and blue ellipses are epicentres of low-frequency earthquakes and source areas of slow slip events (Obara & Hirose 2006), respectively. (a) Coseismic slip distributions associated with the 1944 Tonankai and the 1946 Nankai earthquakes obtained by inversion analyses of seismic data (Ichinose *et al.* 2003; Murotani *et al.* 2006), geodetic data (Ito & Hashimoto 2004) and tsunami data (Baba & Cummins 2005). The unit of contour is m. (b) Slip deficit rate on the plate interface estimated from inversion analyses of GPS data (Miyazaki & Heki 2001; Ito & Hashimoto 2004; Kobayashi & Hashimoto 2006). The unit of contour is cm yr^{-1}.

flow data. On-land data errors were estimated based on the standard errors in Hyndman *et al.* (1995). The average of the observation errors is about ±14 mW m^{-2} (positive values indicate increased heat flow, and the corresponding relation of the order of the positive and negative signs is kept in the following). The initial temperature distribution was modified to fit this uncertainty range for a horizontal distance of 400 km from the trough in model region 6, using trial-and-error. Similar heat flow values were obtained when z_{cont} was set at 48 ∓ 16 km in eq. (16). Based on this range, temperatures on the plate interface were calculated for the eight margin-normal profiles, and the average uncertainty of their temperatures was estimated. The estimated uncertainties of the 150, 350 and 450 °C isotherm locations were ∓0, ∓3 and ∓13 km (positive values indicate margin-normal landward direction), respectively, measured in the horizontally projected plate interface (Fig. 10). Uncertainty in heat flow data on land affects only the temperatures on the continental side of the plate boundary. The observation errors of BSR heat flow data are about ±5 mW m^{-2} (Ashi, personal communication). The thermal conductivity of the oceanic plate and the mantle and the potential temperature were modified to fit the uncertainty range along the eight margin-parallel profiles near the Nankai Trough. Assuming the uncertainty in the thermal conductivity of the oceanic plate and the mantle to be $2.5 \pm 0.1\,\mathrm{Wm^{-1}\,K^{-1}}$, the uncertainty in the potential temperature was $1300 \pm 75\,^{\circ}$C using trial-and-error. The estimated average uncertainties in the 150, 350 and 450 °C isotherm locations were ∓ 2, ∓ 16 and ∓ 17 km, respectively, measured in the horizontally projected plate interface (Fig. 10).

The model parameters (Table 2) were tested for sensitivity by changing them by ±5 per cent, and changes in the 150, 350 and 450 °C isotherm locations were determined (Fig. 10). A change of $\pm 65\,^{\circ}$C in ΔT, which contributes to Ra_0, ξ and Rh_0, changed the average locations of the eight profiles by ∓ 2, ∓ 9 and ∓ 12 km, respectively. Changing mantle thermal diffusivity, defined by ρ, k and Cp, by $\pm 3.2 \times 10^{-8}\ \mathrm{m^2\ s^{-1}}$ moved the average locations by ∓ 1, ∓ 4 and ∓ 3 km, respectively. Changes in D, Rh_{mantle} and α_0, which also affect Di_0, Γ_0 and ξ, had negligible effects on the average locations. If the continental Moho depth was 30 km, which was 2 km shallower than the depth used in this model, the average locations would change by ∓ 0, ∓ 0 and ∓ 3 km, respectively. We used Christensen's (1996) equation to represent temperature-dependent viscosity, which yielded values ranging from about 10^{19} to 10^{24} Pa s in the range plotted in the figures (e.g. Fig. 7b). To investigate the temperature dependency of viscosity over the temperature field of the subduction fault, two cases with isoviscosity (10^{20} Pa s) and lower temperature-dependent viscosity were calculated; for the latter, the denominator of the temperature term in eq. (10) was changed twice. Comparison of the calculated results for the three cases showed that the effect of temperature-dependent viscosity on the temperature field over the subduction fault was negligible in the depth range from 0 to 32 km.

6 DISCUSSION

6.1 Comparison with Hyndman *et al.* (1995)

Compared with the plate-interface isothermal contours of Hyndman *et al.* (1995), the contours derived using our model exhibit more lateral variation along the trough axis (Fig. 10). This is likely caused by the differences in temperature boundary conditions on the oceanic side and subduction velocity. The temperature at the fossil ridge, the highest along the trough axis, is given as the seaward boundary condition in their 2-D model. This may be the reason why the lower limit of the thermal seismogenic zone (350 °C) in our results coincides well with that of Hyndman *et al.* (1995) in eastern Shikoku. Given that the second term in eqs (18) and (19) is a new factor in our 3-D model, the temperature along the Nankai Trough depends on the distance from the fossil ridge, which has moved westward over the last 5 Myr as a result of oblique subduction. The assumption that the continental plate involved after 5 Ma was the AM plate means that the present subduction velocity off Shikoku is about 2 cm $\mathrm{yr^{-1}}$ faster than the velocity of 4 cm $\mathrm{yr^{-1}}$ assumed in Hyndman *et al.* (1995), who used only one margin-normal profile passing through the eastern part of Shikoku to calculate the temperature distribution. Although they calculated a margin-normal temperature field passing through the Kii Peninsula, the result does not explain the marine BSR data there because the BSR data off western Shikoku were used for data fitting. They also used land-based levelling data from an interseismic interval, from which it would be very difficult to reconstruct the details of the seismogenic zone, considering the variable slip deficit distribution and the poor resolution for locations far off the coasts of Shikoku and the Kii Peninsula.

The downdip limit of the thermal seismogenic zone off the Kii Peninsula as derived using our model is located farther seaward than that of Hyndman *et al.* (1995). This is because of the higher dip angle there and the passage of the hot fossil ridge in the past. The downdip limit of the transition zone (450 °C) is also different, corresponding to the location of the thermal seismogenic zone (350 °C). Our calculated transition zone appears to be wider than that of Hyndman *et al.* (1995). This is probably because the highest temperature condition for the fossil ridge is given in their model at the trough axis, whereas our model incorporated the thermal age dependency in the margin-parallel direction.

The updip limits of the thermal seismogenic zone (150 °C) in the two models are nearly the same within the uncertainty range. Although the age dependency of the subducting plate in the margin-parallel direction was included in our model, which tends to cause longer margin-normal distance of isotherms from the trough axis with increasing distance from the fossil ridge, and not in the previous model, the location of the updip limit from the trough axis is about the same. This is because the effect of age dependency was cancelled by the faster spreading rate, which tends to cause shorter margin-normal distance of isotherms from the trough axis with increasing margin-parallel distance from the fossil ridge. Although Hyndman & Wang (1993) proposed that the updip limit is closely related to the smectite-illite phase transition, Moore & Saffer (2001) indicated that unstable sliding does not take place for transformed illite, but that a decreased pore–pressure ratio, resulting from a decreased dehydration rate caused by progressive metamorphism, causes increased effective normal stress and produces an unstable sliding, or seismogenic zone. Wang & Hu (2006) proposed an idea whereby the actively deforming, most seaward part of an accretionary prism overlies the updip velocity-strengthening part of the subduction fault and the less-deformed inner wedge overlies the velocity-weakening part (seismogenic zone). The parameters controlling the updip limit clearly remain contentious.

6.2 Comparison of temperature distribution and coseismic slip distributions associated with the 1944 Tonankai and 1946 Nankai earthquakes, and interplate coupling

Our results for Shikoku and the Kii Peninsula can be compared with coseismic slip distributions associated with the 1944 Tonankai (M 7.9) and the 1946 Nankai (M 8.0) earthquakes and the distribution of slip deficit rates. The coseismic slip distributions of the two earthquakes inferred from inversion analyses of seismic data (Ichinose *et al.* 2003; Murotani *et al.* 2006), geodetic data (Ito & Hashimoto 2004) and tsunami data (Baba & Cummins 2005) are shown (Fig. 10a). Common characteristics for these results are maximum slip off Shikoku for the Nankai earthquake, and southeast to east of the Kii Peninsula for the Tonankai earthquake. Interestingly, all of these maximum slip areas are located in the deeper part of the thermal seismogenic zone, including the rupture initiation points for the two earthquakes.

The spatial distributions of slip deficit rates have been inferred from inversion analyses of GPS data (e.g. Miyazaki & Heki 2001; Ito & Hashimoto 2004; Kobayashi & Hashimoto 2006; Fig. 10b). The results indicate a strongly coupled region off Cape Muroto, adjacent to the maximum coseismic slip location of the Nankai earthquake. The strongly coupled region is located within the calculated thermal seismogenic zone. From these comparisons, we conclude that the thermal seismogenic zone is more or less consistent with the coseismic slip distributions of the two megathrust earthquakes and with interplate coupling.

6.3 Comparison of temperature distributions and occurrence of low-frequency earthquakes

The epicentre distribution of low-frequency earthquakes determined by the Japan Meteorological Agency and the locations of slow-slip events (Obara & Hirose 2006; Fig. 10) coincide with the calculated temperature range of approximately 400–500 °C. Shelly *et al.* (2006) indicated that low-frequency earthquakes occur on the plate interface in western Shikoku by relocation of their hypocentres. This suggests that they are generated by shear slip rather than fluid flow. Shelly *et al.* (2006) hypothesized that increasing fluid pressure in the oceanic crust just below the transient slip zone may reduce the effective normal stress and enable slip on the plate interface.

The fluid source may be dehydration associated with progressive phase transformation of hydrous minerals in oceanic crust. Hacker *et al.* (2003) showed a phase relation of basalt + H_2O on a pressure–temperature diagram. The most likely phase transformation at 400–500 °C at the hypocentre depths of low-frequency earthquakes (30–45 km) is lawsonite + blueschist + jadeite to amphibole + eclogite, which decreases in water content by about 2.4 wt%. On the north side of the belt-like epicentral region, free water would be used to form hydrous minerals such as serpentine in the mantle wedge (Katsumata & Kamaya 2003). The temperature of 400–500 °C also corresponds to the onset of feldspar plasticity (Scholtz 1990). The fact that transient slow-slip events occur at the same locations as low-frequency tremors (e.g. Obara & Hirose 2006) suggests that stable sliding may take place downdip of the low-frequency earthquakes. The western limit of the low-frequency earthquakes is located in northeastern Kyushu, where temperature and pressure conditions likely change abruptly because of plate subduction with high dip angles and to depths deeper than the Moho (Figs 6 and 10).

6.4 Estimated seismogenic zone and its relation to the occurrence of large interplate earthquakes

Hyndman *et al.* (1997) suggested that the downdip limit of the seismogenic zone is basically determined by temperature. However, the boundary between the continental Moho and the upper surface of the subducting oceanic plate becomes the downdip limit if the temperature there is less than 350–450 °C. Seismic data indicate that continental Moho depths in southwest Japan are 30–33 km (Kurashimo *et al.* 2002; Nakamura 2002; Murakoshi 2003; Sala & Zhao 2004). The downdip limit of the thermal seismogenic zone can, therefore, be determined by the temperature off Shikoku and the Kii Peninsula, whereas on the east side of Kyushu, it is probably limited by the boundary where the 350 °C isotherm on the plate interface is located below the Moho (Fig. 10).

M8-class large interplate earthquakes have occurred off the Kii Peninsula and Shikoku. The calculated results indicate that the seismogenic zone is narrowest off the Kii Peninsula and that the hypocentres of the Tonankai and Nankai earthquakes were located in the calculated thermal seismogenic zone (Fig. 10). Rupture initiation points for the Tonankai and Nankai earthquakes obtained from numerical simulations using the rate- and state-dependent friction law are located off the Kii Peninsula, which is consistent with observations for the two most recent events (Hori *et al.* 2004). Hori *et al.* (2004) attributed the location to high stress arising from a narrow seismogenic zone, which is caused by the area's high dip angle and high convergence rate. In contrast, our results suggest that the narrowness of the seismogenic zone off the Kii Peninsula has two causes: a high dip angle, which means that the subducted slab can be heated rapidly by surrounding hot mantle and that hot material can flow into the corner of the mantle wedge; and recent subduction of the fossil ridge, which has always been the hottest part of the subducting plate. The narrow thermal seismogenic zone may be important in understanding the generation of future Tonankai and Nankai earthquakes, which are expected by the middle of this century.

7 CONCLUSIONS

The construction of a 3-D parallelepiped thermal convection model yielded a temperature distribution scheme for the upper boundary of the subducting PHS plate along the Nankai Trough, southwest Japan. Comparison of the heat flow calculated from the temperature distribution with the observed heat flow indicated that the model results fit the data well. We have five significant conclusions.

(1) The calculated temperature distribution on the plate interface indicates that the updip limit of the seismogenic zone is roughly parallel to the trough axis. This is because two important controls cancel one another out: the age of the subducting PHS plate along the Nankai Trough increases with increasing margin-parallel distance from the fossil ridge, but the spreading rate also becomes faster.

(2) The lower limit of the thermal seismogenic zone is determined by the temperature between the Kii Peninsula and western Shikoku, whereas on the east side of Kyushu, where the 350 °C isotherm on the plate interface is located deeper than the Moho, it is delimited by the boundary line between the continental Moho depth and the upper surface of the subducting PHS plate.

(3) The location of maximum coseismic slip associated with the 1944 Tonankai and the 1946 Nankai earthquakes, and the strongly coupled region estimated from GPS data inversion are located in the thermal seismogenic zone.

(4) Low-frequency earthquakes located in the downdip of the thermal seismogenic zone take place at temperatures of approximately 400–500 °C and may be related to the phase transformation of hydrous minerals in oceanic crust from lawsonite + blueschist + jadeite to amphibole + eclogite, which decreases the water content by approximately 2.4 wt%.

(5) The thermal seismogenic zone is narrowest off the Kii Peninsula as a result of: a high dip angle, which means that the subducted slab can be rapidly heated by surrounding hot mantle and that hot material reaches as far as the corner of the mantle wedge, and recent subduction of the fossil ridge, which has always been the hottest part of the subducting plate. The location of the narrowest thermal seismogenic zone may determine the rupture initiation points for future Tonankai and Nankai earthquakes.

ACKNOWLEDGMENTS

We thank P. J. Tackley for sharing his original source code of mantle convection 'Stag3d'. J. Ashi is greatly acknowledged for kindly providing us with heat flow data estimated from BSR. We also thank two anonymous reviewers and the editor J. Korenaga for their constructive comments, and T. Nakagawa for his kind help on calculation. All the figures were created using the Generic Mapping Tools (GMT) software developed by Wessel & Smith (1998).

REFERENCES

Ando, M., 1975. Source mechanisms and tectonic significance of historical earthquakes along the Nankai Trough, *Tectonophysics,* **27,** 119–140.

Ashi, J., Tokuyama, H. & Taira, A., 2002. Distribution of methane hydrate BSRs and its implication for the prism growth in the Nankai Trough, *Marine Geol.,* **187,** 117–191.

Ashi, J., Tokuyama, H., Ujiie, Y. & Taira, A., 1999. Heat flow estimation from gas hydrate BSRs in the Nankai Trough, Implications for thermal structures of the Shikoku Basin, *Suppl. EOS Trans., AGU,* **80**(46), T12A-02.

Baba, T. & Cummins, P.R., 2005. Contiguous rupture areas of two Nankai earthquakes revealed by high-resolution tsunami waveform inversion, *Geophys. Res. Lett.,* **32,** L08304, doi:10.1029.2004GL022320, 2005.

Baba, T., Hori, T., Cummins, P.R., Kameyama, M., Uhira, K. & Kaneda, Y., 2000. Shape of the Philippine Sea plate estimated from seismic surveys and seismicity, *Prog. Abst. Seismol. Soc. Jpn.,* **B50** (in Japanese).

Chopelas, A. & Boehler, R., 1992. Thermal expansivity in the lower mantle, *Geophys. Res. Lett.,* **19,** 1983–1986.

Christensen, U.R., 1996. The influence of trench migration on slab penetration into the lower mantle, *Earth Planet. Sci. Lett.,* **140,** 27–39.

Currie, C.A., Hyndman, R.D., Wang, K. & Kostoglodov, K., 2002. Thermal models of the Mexico subduction zone: Implications for the megathrust seismogenic zone, *J. Geophys. Res.,* **107,** doi:10.1029/2001B000886.

Dragert, H., Wang, K. & James, T.S., 2001. A silent slip event on the deeper Cascadia subduction interface, *Science,* **292,** 1525–1528.

Furukawa, Y., 1999. Interplate coupling and deformation in the accretionary prism in the Southwest Japan subduction zone, *Geophys. Res. Lett.,* **26,** 3145–3148.

Hacker, B.R., Abers, G.A. & Peacock, S.M., 2003. Subduction factory 1. Theoretical mineralogy, densities, seismic wave speeds, and H_2O contents, *J. Geophys. Res.,* **108,** doi:10.1029/2001JB001127.

Honda, S., 1997. Mantle dymanics II—mechanics, in *Iwanami-koza Earth and Planetary Science 10 Dynamics of the Earth's interior*, Iwanami-Shoten, Tokyo, pp. 73–121 (in Japanese).

Hori, T., Kato, N., Hirahara, K., Baba, T. & Kaneda, Y., 2004. A numerical simulation of earthquake cycles along the Nankai Trough in southwest Japan: lateral variation in frictional property due to the slab geometry controls the nucleation position, *Earth Planet. Sci. Lett.,* **228,** 215–226.

Hyndman, R.D. & Wang, K., 1993. The rupture zone of Cascadia great earthquakes from current deformation and the thermal regime, *J. Geophys. Res.,* **98,** 2039–2060.

Hyndman, R.D., Wang, K. & Yamano, M., 1995. Thermal constraints on the seismogenic portion of the southwestern Japan subduction thrust, *J. Geophys. Res.,* **100,** 15 373–15 392.

Hyndman, R.D., Yamano, M. & Oleskevich, D.A., 1997. The seismogenic zone of subduction thrust faults, *Island Arc.,* **6,** 244–260.

Ichinose, G.A., Thio, H.K., Somerville, P.G., Sato, T. & Ishii, T., 2003. Rupture process of the 1944 Tonankai earthquake (Ms 8.1) from the inversion of teleseismic and regional seismograms, *J. Geophys. Res.,* **108,** doi:10.1029/2003JB002393.

Ito, T. & Hashimoto, M., 2004. Spatio-temporal distribution of interplate coupling in southwest Japan deduced from inversion analysis, *J. Geophys. Res.,* **109,** B02315, doi:10.1029/2002JB002358.

Iwamori, H., 1997. Heat sources and melting in subduction zones, *J. Geophys. Res.,* **102,** 14 803–14 820.

Katsumata, A. & Kamaya, N., 2003. Low-frequency continuous tremor around the Moho discontinuity away from volcanoes in the southwest Japan, *Geophys. Res. Lett.,* **30,** 1020, doi:10.1029/2002GRL015981.

Kobayashi, T. & Hashimoto, M., 2006. Estimate of interplate coupling along the Nankai Trough by using a new plate model, Abstr. Japan Geoscience Union Meeting, S208–011.

Kobayashi, K. & Nakada, M., 1978. Magnetic anomalies and tectonic evolution of the Shikoku Inter-arc Basin, *J. Phys. Earth,* **26**(Suppl.), s392–402.

Kodaira, S. *et al.*, 2002. Structure factors controlling the rupture process of a megathrust earthquake at the Nankai trough seismogenic zone, *Geophys. J. Int.,* **149,** 815–835.

Kurashimo, E. *et al.*, 2002. Geometry of the subducting Philippine Sea plate and the crustal and upper mantle structure beneath eastern Shikoku island revealed by seismic refraction/wide-angle reflection profiling, *Zisin,* **54,** 489–505 (in Japanese with English abstract).

Mats, V.D., 1993. The structure and development of the Baikal rift depression, *Earth-Sci. Rev.,* **34,** 81–118.

Miyazaki, S. & Heki, K., 2001. Crustal velocity field of southwest Japan: subduction and arc-arc collision, *J. Geophys. Res.,* **106,** 4305–4326.

Moore, J.C. & Saffer, D., 2001. Updip limit of the seismogenic zone beneath the accretionary prism of southwest Japan: an effect of diagenetic to low-grade metamorphic processes and increasing effective stress, *Geology,* **29,** 183–186.

Murakoshi, T., 2003. Seismic structure of the crust and uppermost mantle beneath Kyushu as inferred from receiver function analysis, *Ph. D. thesis*. Kyushu University, Japan, 105pp.

Murotani, S., Shimazaki, K., Koketsu, K., Furumura, T., Baba, T. & Cummins, P., 2006. Source process of the 1946 Nankai earthquake estimated from inversion of teleseismic waveforms, *Abstr. Japan Geosci. Union Meeting,* S117–001.

Nakamura, M., 2002. Estimate of Moho discontinuity by using converted wave in seismograms of intermediate earthquakes beneath the Kyushu district, Japan, *Master thesis,* Kyushu University, Japan.

Nakamura, M., Watanabe, H., Konomi, T., Kimura, S. & Miura, K., 1997. Characteristic activities of subcrustal earthquakes along the outer zone of southwestern Japan, *Annu. Disas. Prev. Res. Inst., Kyoto Univ.,* **40,** 1–20 (in Japanese with English abstract).

Obara, K., 2002. Nonvolcanic deep tremor associated with subduction in southwest Japan, *Science,* **296,** 1679–1681.

Obara, K. & Hirose, H., 2006. Non-volcanic deep low-frequency tremors accompanying slow slips in the southwest Japan subduction zone, *Tectonophysics,* **417,** 33–51.

Okino, K., Shimakawa, Y. & Nagaoka, S., 1994. Evolution of the Shikoku Basin, *J. Geomag. Geoelectr.,* **46,** 463–479.

Oleskevich, D.A., Hyndman, R.D. & Wang, K., 1999. The updip and downdip limits to great subduction earthquakes: thermal and structural models of Cascadia, south Alasca, SW Japan, and Chile, *J. Geophys. Res.,* **104,** 14 965–14 991.

Rogers, G. & Dragert, H., 2003. Episodic tremor and slip on the Cascadia subduction zone: the chatter of silent slip, *Science,* **300,** 1942–1943.

Sala, H. & Zhao, D., 2004. Mapping the crustal thickness in southwest Japan using Moho-reflected waves, *Phys. Earth Planet. Inter.,* **141,** 79–94.

Sandwell, D.T. & Smith, W.H.F., 2001. *Bathymetric estimation, in Satellite Altimetry and Earth Sciences*, International Geophysics Series, 69, Academic Press, San Diego, pp. 441–457.

Scholtz, C.H., 1990. *The Mechanics of Earthquakes and Faulting*, Cambridge University Press, New York, 439 pp.

Sella, G.F., Dixon, T.H. & Mao A., 2002. REVEL: a model for Recent plate velocities from space geodesy, *J. Geophys. Res.,* **107,** doi: 10.1029/2000JB000033.

Seno, T. & Maruyama, S., 1984. Paleogeographic reconstruction and origin of the Philippine Sea, *Tectonophysics,* **102,** 53–84.

Seno, T. & Yamasaki, S., 2003. No low-frequency tremor implying no dehydration and infrequent great interplate earthquakes, *Geophys. Res. Lett.,* **30,** 2171, doi:10.1029/2003GRL018349.

Shelly, D.R., Beroza, G.C., Ide, S. & Nakamula, S., 2006. Low-frequency earthquakes in Shikoku, Japan, and their relationship to episodic tremor and slip, *Nature,* **442,** 188–191.

Shimizu, H., Uehira, K., Matsushima, T., Matsuo, N., Fukui, R., Yakiwara, H. & Goto, K., 2000. The detailed structure of deep seismic zone in the Kyushu district, 95–118, in Research on seismotectonics at a high-dip subduction zone based on marine and land observation, Research report (In Japanese with English abstract).

Smolarkiewicz, P.K., 1984. A fully multidimensional positive definite advection transport algorithm with small implicit diffusion, *J. Comput. Phys.,* **54,** 325–362.

Tackley, P.J., 1996. Effects of strongly variable viscosity on three-dimensional compressible convection in planetary mantles, *J. Geophys. Res.,* **101,** 7711–7772.

Takahashi, M., 2004. The cause and timing of E-W contraction of the Japanese Islands, *Prog. Abstr. Seismol. Soc. Japan,* Fall Meeting, B048 (in Japanese).

Tanaka, A., Yamano, M., Yano, Y. & Sasada, M., 2004. Geothermal gradient and heat flow data in and around Japan, digital geoscience map DGM P-5, Geological Survey of Japan.

Wang, K., 2000. Stress-strain 'paradox', plate coupling, and forearc seismicity at the Cascadia and Nankai subduction zones, *Tectonophysics,* **319,** 321–338.

Wang, K. & Hu, Y., 2006. Accretionary prisms in subduction earthquake cycles: the theory of dynamic Coulomb wedge, *J. Geophys. Res.,* **111,** B06410, doi:10.1029/2005JB004094.

Wang, K., Hyndman, R.D. & Yamano, M., 1995. Thermal regime of the Southwest Japan subduction zone: effects of age history of the subducting plate, *Tectonophysics,* **248,** 53–69.

Wei, D. & Seno, T., 1998. Determination of the Amurian plate motion, in mantle dynamics and plate interactions in East Asia, Geodynamics Series, 27, American Geophysical Union, Washington, D.C., pp. 337–346.

Wessel, P. & Smith, W.H.F., 1998. New, improved version of the Generic Mapping Tools released, *EOS Trans., AGU,* **79,** 579.

Yoshii, T., 1975. Regionality of group velocities of Rayleigh waves in the Pacific and thickening of the plate, *Earth Planet. Sci. Lett.,* **25,** 305–312.

Yoshioka, S. & Ito, Y., 2001. Lateral variations of effective elastic thickness of the subducting Philippine Sea plate along the Nankai trough, *Earth Planets Space,* **53,** 261–273.

Yoshioka, S. & Sanshadokoro, H., 2002. Numerical simulations of deformation and dynamics of horizontally lying slabs, *Geophys. J. Int.,* **151,** 69–82.